

# Autonomously Adhesive, Stretchable, and Transparent Solid-State Polyionic Triboelectric Patch for Wearable Power Source and Tactile Sensor

Zhiqing Bai, Yunlong Xu, Chengkuo Lee,\* and Jiansheng Guo\*

Robust power supplies and self-powered sensors that are extensible, autonomously adhesive, and transparent are highly desirable for next-generation electronic/energy/robotic applications. In the work, a solid-state triboelectric patch integrated with the above features ( $\approx 318\%$  elongation,  $>85\%$  average transmission,  $\approx 44.3 \text{ N m}^{-1}$  adhesive strength) is developed using polyethylene oxide/waterborne polyurethane/phytic acid composite (abbreviated as PWP composite) as an effective current collector and silicone rubber as tribolayer. The PWP composite is optimized systematically and corresponding single-electrode device can supply a power density of  $2.3 \text{ W m}^{-2}$  at  $75\%$  strain. The triboelectric patch is capable of charging capacitors and powering electronics by efficiently harvesting biomechanical energies. Moreover, it can be autonomously attached to nonplanar skin or apparel substrates and used as a tactile sensor or an epidermal input touchpad for physiological motion detection and remote control of appliances, respectively. Even after dynamic deformation, tailoring, and prolonged use, the patch can maintain good stability and reliability of electrical outputs. This work provides a novel solid-state and liquid-free polyionic electrode-based triboelectric nanogenerator integrated with adhesiveness, stretchability, and transparency, which can meet wide application needs from transparent electronics, artificial skins, to smart interfaces.

prosthetic/robotic/energy skins,<sup>[8–10]</sup> and optoelectronic devices,<sup>[11–13]</sup> especially in multifunctional integrated devices with deformability, transparency, and adhesiveness, etc. The features of extensibility and stretchability allow the close assembly to nonplanar skin for realizing conformability between human body and frequent human movements. The transparency of device can open up the possibility of integrating it into wearable user-interactive display and smart clothing, so as to display information without affecting their original appearance attributes and obstructing the view.<sup>[14,15]</sup> Moreover, the transparency of device can satisfy the aesthetic requirements of next-generation electronics. Additionally, good adhesiveness can realize autonomous attachment to various substrates without additional adhesives. Importantly, the combination of adhesiveness and stretchability allows the device to deform freely under complex movements and avoids interfacial delamination from substrates in practical application. Therefore, developing flexible compatible

energy devices with multiple features is highly desirable for next-generation electronics.

As an energy harvesting technology, TENG based on triboelectrification and electrostatic induction has attracted much attention because of their inherent advantages of diverse work modes, material operation freedom, and high conversion efficiency.<sup>[16,17]</sup> TENG can continually transfer ubiquitous mechanical energies to electrical signals, which is considered as an ideal candidate for sustainable power source.<sup>[18,19]</sup> Moreover, the electrical pulse generated from TENG can be used as an effective feedback signal to reveal and differentiate the attributes of external stimuli, showing great potential in self-powered tactile sensors with no extra power.<sup>[10,20,21]</sup> However, TENGs used for power source and tactile sensor mostly used metal materials as current collectors, resulting in the nonextensibility of devices. To this end, in recent years, many efforts have focused on the development of deformable electrodes, such as elastic polymers embedded with conductive fillers (Ag nanowire,<sup>[22,23]</sup> carbon nanotube,<sup>[24,25]</sup> etc.), ionic conductors,<sup>[26–29]</sup> liquid metals,<sup>[30,31]</sup> and liquid electrolytes.<sup>[32]</sup> Although nanofiller conductive composites can realize remarkable stretchability of TENGs, they suffer from break degradation of percolation networks and a sharp decrease in conductivity

## 1. Introduction

The Internet of Things (IoT) and Artificial Intelligence (AI) have accelerated the rapid growth of next-generation electronics, such as wearable power sources,<sup>[1,2]</sup> tactile sensors,<sup>[3–7]</sup>

Dr. Z. Bai, Dr. Y. Xu, Prof. J. Guo  
Key Laboratory of Textile Science and Technology  
Ministry of Education  
College of Textiles  
Donghua University  
Shanghai 201620, China  
E-mail: jsguo@dhu.edu.cn

Dr. Z. Bai, Prof. C. Lee  
Department of Electrical and Computer Engineering  
Center for Intelligent Sensors and MEMS (CISM)  
and NUS Graduate School for Integrative Sciences and Engineering  
National University of Singapore  
Singapore 117576, Singapore  
E-mail: elelc@nus.edu.sg

 The ORCID identification number(s) for the author(s) of this article can be found under <https://doi.org/10.1002/adfm.202104365>.

DOI: 10.1002/adfm.202104365

during stretching. And these devices also lack sufficient transparency because of the doping of nanofillers. Comparatively, hydrogels or ionogels composed of cross-linked polymer networks and ionic conductors (salts and ionic liquid) are more tolerant of large deformation and are transparent for the full visible spectrum. These gels are widely used as electrodes to construct deformable and transparent wearable TENGs. For example, Kim et al. proposed catechol-chitosan-diatom hydrogel and used it as a stretchable and adhesive electrode in TENG for human motion energy harvesting and the health monitoring of Parkinson's disease patients.<sup>[33]</sup> Wang et al. developed the chitosan-based hybrid conductive hydrogel as current collector for washable power source and self-powered temperature-stress dual sensor.<sup>[34]</sup> Unfortunately, hydrogel-based TENGs are less environmentally stable because their mechanical toughness and conductivity deteriorate with hydrogel dehydration or liquid solvent evaporation, which eventually leads to the failure of devices. Additionally, the ionic liquids tend to escape from conductive ionogels, which results not only in performance degradation of devices but also in an adverse effect on human health. And ionogels are nonadhesive due to the lack of functional groups for bonding and thus need to be fixed on target substrates with the aid of additional binders. Very recently, Wang, et al. have proposed a stretchable and shape adaptable TENG using potassium iodide and glycerol liquid electrolyte as work electrode.<sup>[32]</sup> The device exhibits desirable tensile property and electrical output; however, the liquid electrolyte leakage is also an issue of great concern. Therefore, it is still a challenge to develop robust solid-state TENG integrated multiple characteristics as power sources or self-powered sensors to meet the rapidly growing demand for wearable electronics.

Herein, a solid-state and liquid-free triboelectric patch using PWP polyionic composite as an effective current collector is designed. The PWP composite is formed through the hydrogen bonding cross-linking among polyethylene oxide (PEO), waterborne polyurethane (WPU), and phytic acid (PA). The collaboration of PWP polyionic electrode and silicone rubber tribolayer endows the patch with good stretchability, transparency, and autonomous adhesion. The effect of thickness of PWP composite and the content of PA on electrical performance are investigated and the optimal device is capable of generating high electrical outputs with  $V_{OC}$  of 197 V,  $J_{SC}$  of 17.3  $\mu\text{A}$ , and instantaneous power density of 2.3  $\text{W m}^{-2}$ . Meanwhile, the triboelectric patch can keep stable and reliable electrical performance under diverse stretching/twisting/folding deformations and repeated operations for 10 000 cycles. As a result of these advantages, the patch can be attached autonomously to clothes or human skin without binding agent for powering microdevices, monitoring physiological signals, and controlling electrical appliances, implying potential applications in self-powered electronics and wearable interactive systems.

## 2. Results and Discussion

### 2.1. Fabrication and Characterization

Figure 1a describes the 3D structure of solid-state triboelectric patch, which is composed of layers of adhesive polyionic composite and electronegative silicone rubber. The fabrication

process is depicted in Figure 1b. Briefly, the PWP composite as an effective current collector was prepared by casting the mixture consisting of PEO (Figure 1a-i), PA (Figure 1a-ii), and WPU (Figure 1a-iii) polymers. Although PEO is one of the most commonly used polymer electrolytes, it is a semicrystalline thermoplastic polymer with limited extensibility and nonadhesion. Eco-friendly WPU can well mix with PEO polymer, leading to a decrease in crystallinity and an enhancement in stretchability. Moreover, the introduction of PA biomolecules with negatively charged phosphate groups as conductive dopants and crosslinking agents can not only endow PWP composite with high ionic conductivity but also improve its adhesiveness to substrates. As a biocompatible elastomer, silicone rubber is usually used as tribomaterial or encapsulation because of its electronegativity, good elasticity, and optical transparency.<sup>[35,36]</sup> Thus, the top surface of PWP composite was subsequently covered by the low-temperature vulcanized (LTV) silicone rubber as an effective negative tribolayer (Figure 1b-iii) and finally the polyionic triboelectric patch was obtained after curing (Figure 1a). It is interesting to note that when the LTV tribolayer was lifted away from the pre-prepared groove model, the PWP composite could also be peeled off together. This is because the functional groups distributed on the surface of PWP composite and seamless contact ensure a stable bonding for the PWP/LTV interface. Preparation details can be found in the Experimental Section. This kind of triboelectric patch can realize sustainable power supply, self-powered tactile sensing, and smart control through a transformation of external stimulus into an electrical pulse.

The triboelectric patch exhibits superior optical transparency in the visible range. As displayed in Figure 2a, the colorful holiday flags covered with triboelectric patch and LTV film are observed and distinguished. The corresponding transmittance spectra were examined in Figure 2b and Figure S1 (Supporting Information). The average transmittance of triboelectric patches with different PWP composites within a visible range is over 85%, which is slightly lower than that of pure LTV film (91%). This also indirectly proves the good transparency of PWP composite. X-ray diffraction (XRD) patterns were further carried out for revealing phase structure. As shown in Figure 2c, compared with semicrystalline PEO film, the intensity of two characteristic peaks at  $2\theta = 19.1^\circ$ ,  $23.1^\circ$  in the PEO/WPU curve is weakened visibly, while the peak shape is widened. This illustrates that more disordered arrangements of molecular frameworks in the PEO/WPU film are generated after the incorporation of WPU. However, due to the introduction of PA molecules, the XRD pattern of PWP composite only exhibits a single broad diffraction peak instead of two sharp peaks, indicating the less ordered arrangement and lower crystallinity than that of PEO/WPU film. This change is attributed to rich intermolecular hydrogen bonding interactions among PEO, WPU, and PA polymer chains.<sup>[37]</sup> These XRD results also confirm the good transparency of PWP composite because lower crystallinity contributes to the increased transmittance.<sup>[38]</sup> Moreover, to reveal the interfacial adhesion state between top LTV tribolayer and bottom PWP composite, the morphology of triboelectric patch was characterized. Figure 2d presents the cross-section of triboelectric patch with a layered structure. And the bottom PWP composite is tightly bonded with the top LTV tribolayer and there is no interface gap, which allows the triboelectric patch to

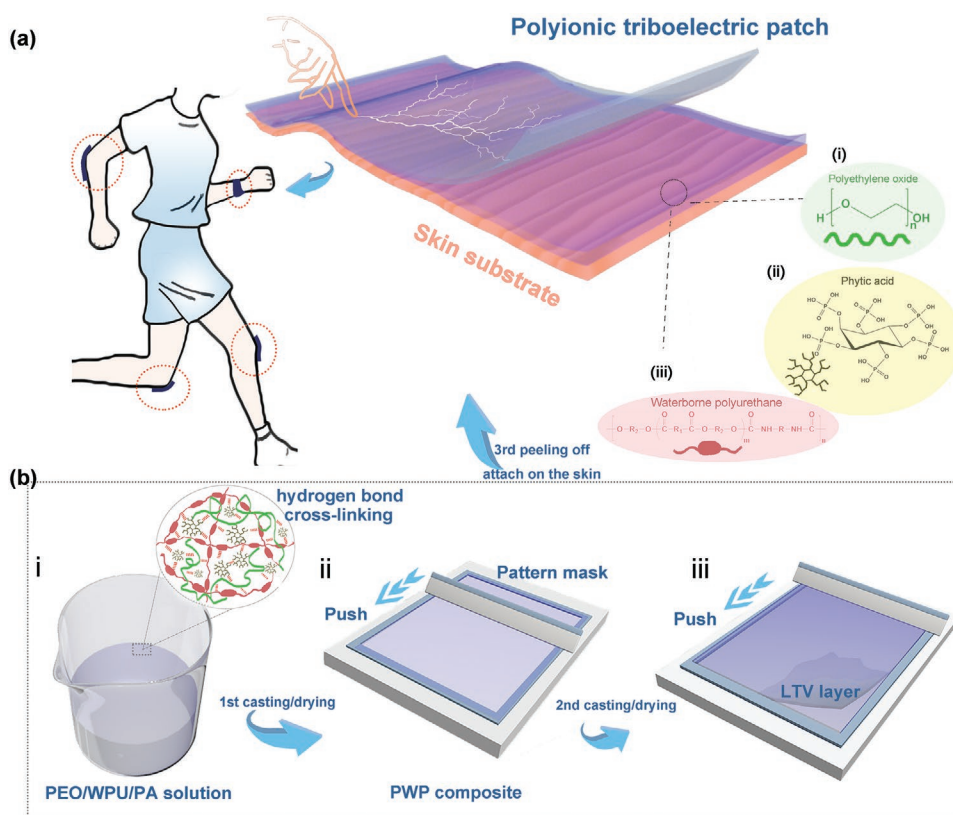


**Figure 1.** Schematic illustration for the preparation of polyionic triboelectric patch. a) The patch structure consisting of PWP current collector and silicon rubber tribolayer. Chemical structures of PEO (a-i), PA (a-ii), and WPU (a-iii). b) Preparation of the polyionic triboelectric patch: mixing of PEO, WPU, and PA molecules (b-i); drop-casting homogeneous mixture in a homemade mold (b-ii); covering of silicon rubber tribolayer (b-iii).

keep integrity in practical application. Energy dispersive spectroscopy (EDS) mapping analysis was used to check the formation of the PWP composite in Figure 2e and Figure S2 in the Supporting Information. Elements C, O, N, and P are found to be evenly distributed, indicating the uniform blend of PEO, WPU, and PA molecules in the PWP composite. Additionally, Figure S3 (Supporting Information) presents the measured water contact angle of  $115^\circ$  for the triboelectric patch, which implies less sensitivity to water molecules and good stability in a humid environment.<sup>[39]</sup>

The mechanical properties of triboelectric patch, such as deformability and extensibility, are the basic requirement for wearability. Figure 2f and Video S1 (Supporting Information) show that the patch is easy to be repeatedly stretched at different strains, with necking phenomenon but no fracture, exhibiting good mechanical stretchable behavior. This may be attributed to the synergy between highly entangled molecular chains resulting from hydrogen bond cross-linking in PWP composite (Figure 1b-i; Figure S4, Supporting Information), silicone rubber cross-linking network, and WPU soft segments.<sup>[35,40–44]</sup> Further, stress–strain curves of triboelectric patch, PEO, and PEO/WPU membranes were measured, as shown in Figure 2g. The triboelectric patch exhibits a mechanical strength of 3.2 MPa and a breaking elongation of 318%. And compared with the PEO film, Young's modulus of the patch decreases by 99%, and elongation at break increases by 4971% (Figure S5, Supporting Information). This variation implies that triboelectric

patches can better adapt to complex deformation motions of human body and form conformal contact with human skin. Note that the strain to fracture of PEO/WPU film is as high as 608%, much higher than that of pristine PEO film, which illustrates the great contribution of WPU molecular chains in elongation. Moreover, the fatigue hysteresis was measured to evaluate the elastic property, as shown in Figure 2h. Although hysteresis in the first cycle is observed, the triboelectric patch exhibits almost coincidental hysteresis loops from the second to the eleventh cycle, which indicates good fatigue resistance in multiple loading–unloading processes.

## 2.2. Autonomously Adhesive Properties

The solid-state polyionic triboelectric patch is also endowed with adhesiveness property, allowing it to adhere to target surfaces without adhesive tapes or glues. As shown in Figure 3a, even if the patch is stretched when the index finger bends forward, it can still adhere well to the skin without a trace of shedding. When the wrist moves from straight state to bending angles of  $30^\circ$  and  $60^\circ$ , the triboelectric patch always maintains seamless interface adhesion with delicate curved skin on the back of the wrist (Figure 3b). Moreover, the conformal contact between triboelectric patch and latex balloon is observed in the dynamic inflation/deflation process. As demonstrated in Figure 3c and Video S2 in the Supporting Information,

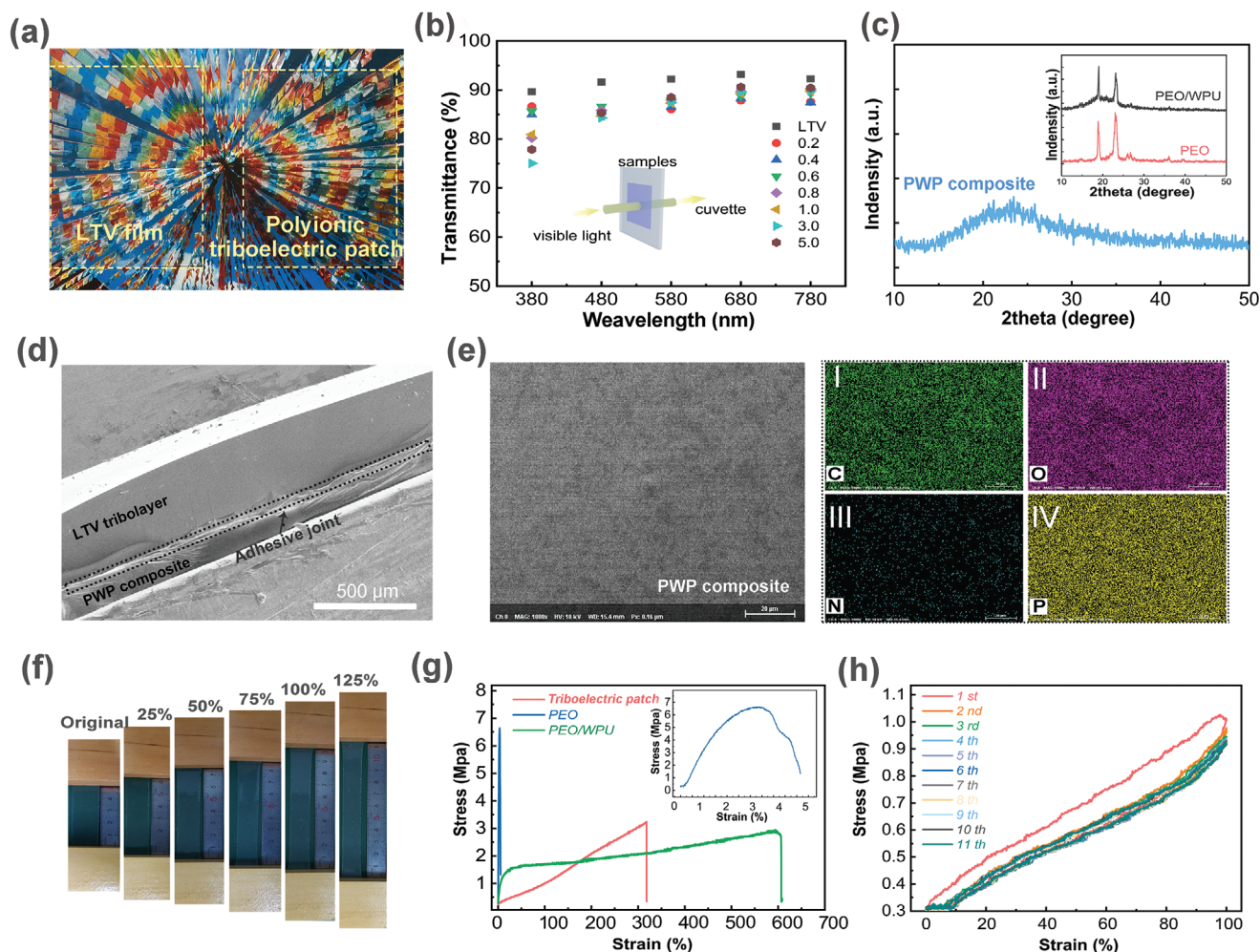


**Figure 2.** Characterization and mechanical properties of polyionic triboelectric patch. a) Photos of the patch and LTV film with good transparency. b) The image showing the transmittance of LTV and triboelectric patches with different PA content (0.2, 0.4, 0.6, 0.8, 1.0, 3.0, 5.0 mL) at different wavelengths. The inset showing the measurement schematic. c) XRD patterns of PWP, PEO, and PEO/WPU films. d) Microscopic image of cross-section of the patch. e) Images of surface topography and elemental mapping. f) The stretchability of the patch. g) Comparison of stress–strain curves of PEO, PEO/WPU, triboelectric patch. h) Cycling tensile curves of the triboelectric patch in successive 11 cycles.

the patch can deform multi-directionally in the balloon inflation and restore to initial state in the deflation process. Simultaneously, the red letters “DHU” covered with the patch are clearly observed. This demonstration perfectly illustrates good dynamic multidirectional adhesion, extensibility, and transparency of triboelectric patches. The substrate adhesive strength of triboelectric patch was further revealed using standard 90° peel tests. As shown in Figure 3d and Figure S6 (Supporting Information), the patch exhibits considerable peeling force for various substrates. Particularly, the patch displays the highest adhesive strength ( $44.3 \text{ N m}^{-1}$ ) to silk fabric, followed by other fabrics, PET plastic, paper, rubber, and PTFE plastic. Figure 3e and Video S3 (Supporting Information) also intuitively show that diverse substrates can be firmly pasted to polystyrene foam using triboelectric patch, even though they are heavily disturbed by the wind.

The substrate adhesion mechanism can be explained by the synergistic effect of physical adsorption and mechanical interlocking between PWP composite and substrate.<sup>[45,46]</sup> First, FTIR

spectra of PWP, WPU, PA, and PEO membranes were revealed in Figure 3f and Figure S7 (Supporting Information). The PWP spectrum exhibits strong absorption bands centered at 3340, 1736, 961, and  $480 \text{ cm}^{-1}$ , resulting from the stretching vibration of N–H and O–H groups of WPU and PA, C=O groups of WPU, P–OH groups of PA molecular chains, respectively.<sup>[37,47]</sup> Particularly, the peak at  $3340 \text{ cm}^{-1}$  in PWP spectrum has shifted towards lower frequencies, which implies the presence of intermolecular hydrogen bond cross-linking among amino or carboxyl groups of WPU, hydroxyl groups of PA, and ether oxygen groups of PEO polymer chains.<sup>[40–42]</sup> Compared with pure PA, the 961 and  $480 \text{ cm}^{-1}$  bands have shifted to higher wavenumbers, indicating that hydrogen bonds among hydroxy groups of PA molecules were partly detached and additional hydrogen bonds cross-linking were formed in PWP composite.<sup>[48]</sup> These abundant groups distributed on the surface of PWP composite are easy to form strong physical adsorption on various substrates, which endows the patch with strong adhesion property.<sup>[46]</sup> For example, amino, hydroxyl, carbonyl, and ether oxygen groups can form hydrogen

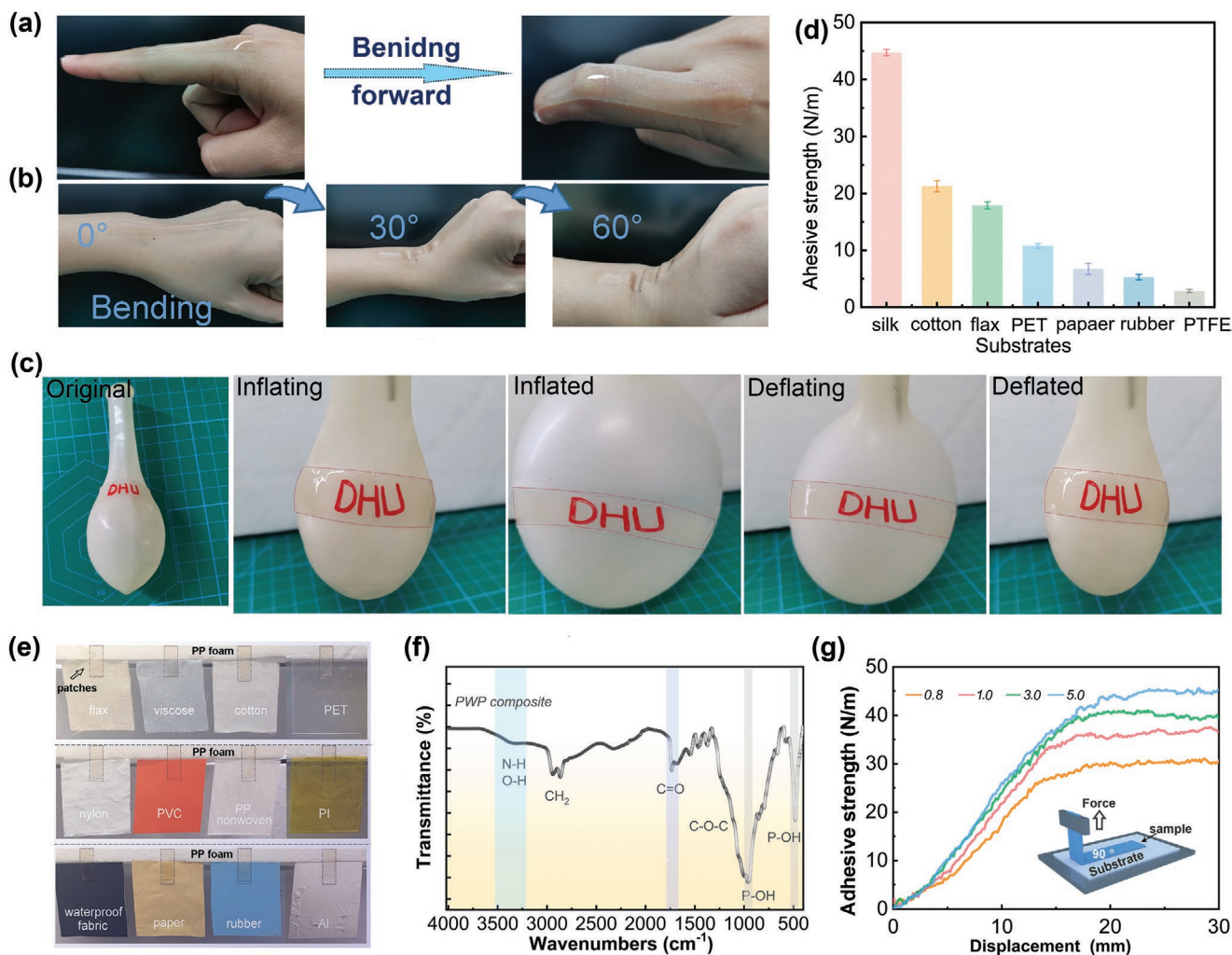


**Figure 3.** Adhesiveness and conformability of the polyionic triboelectric patch. a) Digital photo of conformal contact to the bent index finger. b) Photograph demonstrating attachability of the patch on the delicate skin at different bending angles of wrist. c) Optical images of the patch multidirectionally deformed with the balloon inflation and deflation. d) Interfacial toughness of the patch to various substrates. e) Photos showing that diverse substrates can be adhered to the foam substrate using patch strips. f) FTIR spectra for explaining the adhesion mechanism. g) Interfacial adhesive strength of patch with different PWP composites. The illustration is a setup diagram of the standard 90° peel test.

bonding with N, O, and F components of substrates.<sup>[46]</sup> And carbonyl, ether oxygen, and phosphate groups may produce metal complexation with metal substrates. The PWP composite may also bond to substrates through electrostatic interactions.<sup>[49]</sup> In addition to these physical interactions, the PWP composite can penetrate porous substrates for generating mechanically interlocked structures (Figure S8, Supporting Information).<sup>[45]</sup> Therefore, the strong adhesion between triboelectric patch and silk fabric is mainly ascribed to the porous structure of silk fabric and the physical interaction of functional groups (Figure 3d). It is noteworthy that the adhesive strength of triboelectric patch is largely dependent on the PA content of PWP composite. As shown in Figure 3g and Figure S9 (Supporting Information), the peel force gradually increases with the introduction of PA content from 0.8 to 5 mL, which is primarily related to abundant hydroxyl groups of PA molecules. Nevertheless, when the PA content is less than 0.8 mL, the corresponding patch shows no adhesion behavior.

### 2.3. Optimization on the Electrical Output Performance

The solid-state triboelectric patch is based on the coupling effect of contact electrification and electrostatic induction. When the PWP composite is connected to the ground, it can work in single-electrode mode, as schematically illustrated in Figure 4a. When dielectric is in contact with LTV tribolayer, the triboelectrification effect will occur. The negative charges are accumulated on the LTV tribolayer, while positive charges on the dielectric (Figure 4a-i). At the moment, mobile positive and negative ions are randomly distributed in the PWP current collector. As shown in Figure 4a-ii, and iii, when two tribolayers are separated from each other, unscreened negative charges on the LTV tribolayer will induce the accumulation of positive ions at PWP/LTV interface. Subsequently, an electrical double-layer is formed at the PWP/copper interface, with the same number of negative ions. To keep electrostatic equilibrium, free electrons flow from copper wire to the ground

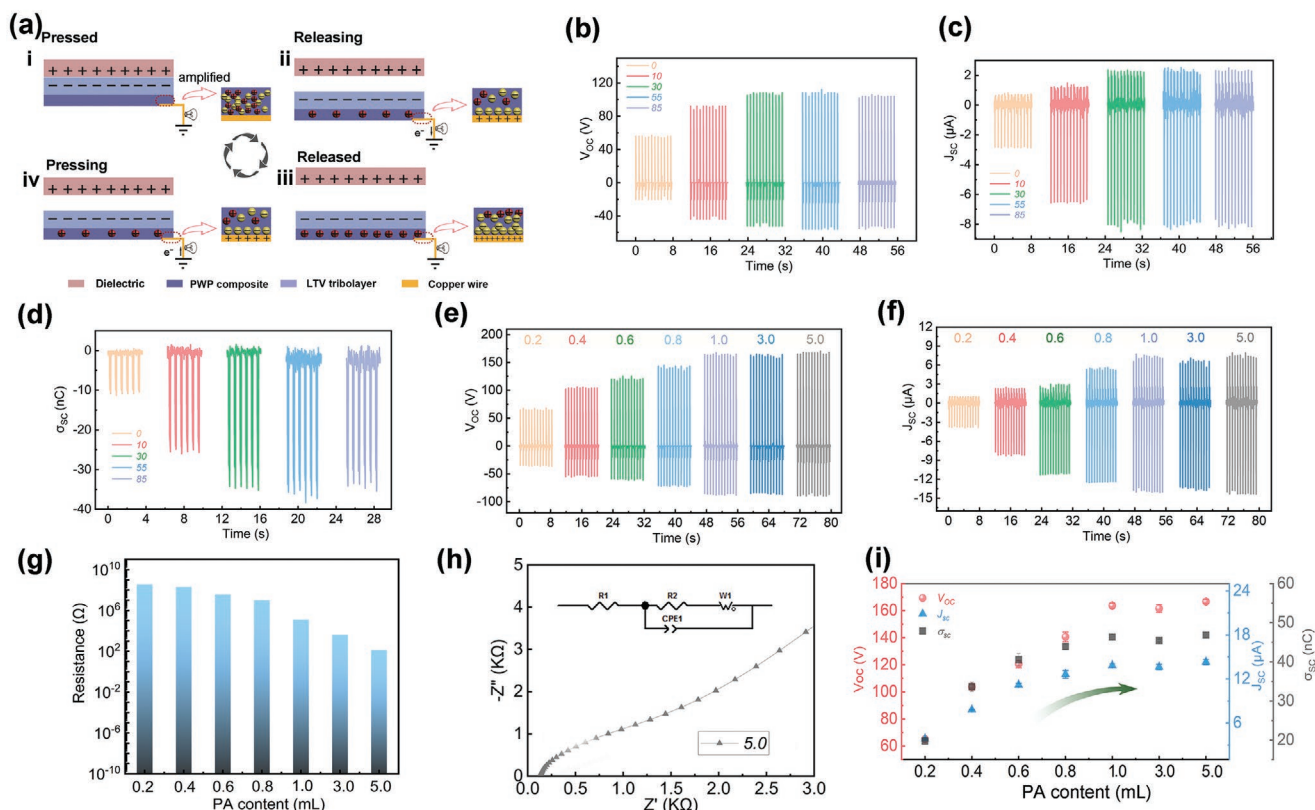


**Figure 4.** Working mechanism and electrical performance optimization of the polyionic triboelectric patch. a) Schematic of the electricity generation mechanism. b) The  $V_{OC}$ , c)  $J_{SC}$ , and d)  $\sigma_{SC}$  outputs of devices with different thicknesses of PWP composite. e) The  $V_{OC}$ , f)  $J_{SC}$  outputs of patches with different PA contents. g) The resistance of PWP composite with different PA contents. h) EIS measurement of PWP composite with 5 mL PA content. i) Curves demonstrating the relationship between electrical outputs and PA content.

through the external circuit, generating an output of electrical output (Figure 4a-ii). Once the dielectric approaches the triboelectric patch again, electrons will return in an inverse way (Figure 4a-iv). As a result, continuous alternating electrical signals will be generated through repeated contact–separation movements.

To obtain high-performance triboelectric patch, a series of PWP composites with different thicknesses were fabricated for preparing triboelectric patches, and the corresponding electrical outputs were measured, as shown in Figure 4b–d. The triboelectric patch without PWP composite (i.e., with only copper wire electrode) can provide the output  $V_{OC}$  of 55 V,  $J_{SC}$  of 2.8  $\mu\text{A}$ , and  $\sigma_{SC}$  of 11 nC. With the thickness of PWP composite increasing from 10 to 85  $\mu\text{m}$ , the outputs of devices increase and then reach a stable value. The triboelectric patch with the PWP thickness of 85  $\mu\text{m}$  can generate  $V_{OC}$  of 104 V,  $J_{SC}$  of 8.0  $\mu\text{A}$ , and  $\sigma_{SC}$  of 34 nC, which are about 90%, 186%, and 209% higher than those of the device with only copper wire electrode, respectively (Figure S10, Supporting Information). This is because that there are more mobile ions distributed along with the cross-linked networks in thicker PWP composite, which can lead to the formation of continuous ionic channels.<sup>[50]</sup> Besides, the contact area between triboelectric patch and PWP polyionic electrode at tribolayer/electrode interface is much larger than that of the device with only copper wire electrode. More ionic channels and larger contact area allow a more sufficient

electrostatic induction and thus more free electrons will flow into the external circuit, leading to an enhancement in electrical outputs.

Further, the effect of PA content on electrical output was also investigated systematically. As shown in Figure 4e,f, when the PA usage increases to 1 mL, the output  $V_{OC}$  and  $J_{SC}$  of the triboelectric patch are greatly enhanced, which may be ascribed to the sharp increase and fast movement of mobile ions in the PWP composite.<sup>[50,51]</sup> The resistance of PWP composites from the Nyquist plots of electrochemical impedance spectra was measured in Figure 4g. When the PA content increases from 0.2 to 1 mL, the resistance of PWP composites decreases sharply from several hundred Megohms to over a hundred Kohms (from  $3.65 \times 10^8$  to  $1.18 \times 10^5 \Omega$ ), showing a change of three orders of magnitude. Thus, the electrical output is greatly dependent on the PA content in the case. Low resistance will lead to a fast and sufficient electrostatic induction of devices, resulting in more free electrons flowing into the external circuit. However, with further increase of PA content, the devices show relatively stable outputs. This is because the impedance of corresponding PWP composites varies within the range of Kohms and ohms and the effect of resistance on electrical outputs can be ignored due to the large inherent impedance of triboelectric patch (M $\Omega$ ). The PWP composite with the PA content of 5 mL exhibits good ionic conductivity of  $7.04 \times 10^{-6} \text{ S m}^{-1}$ , as shown in Figure 4h. And when the composite is connected to the circuit as a wire,

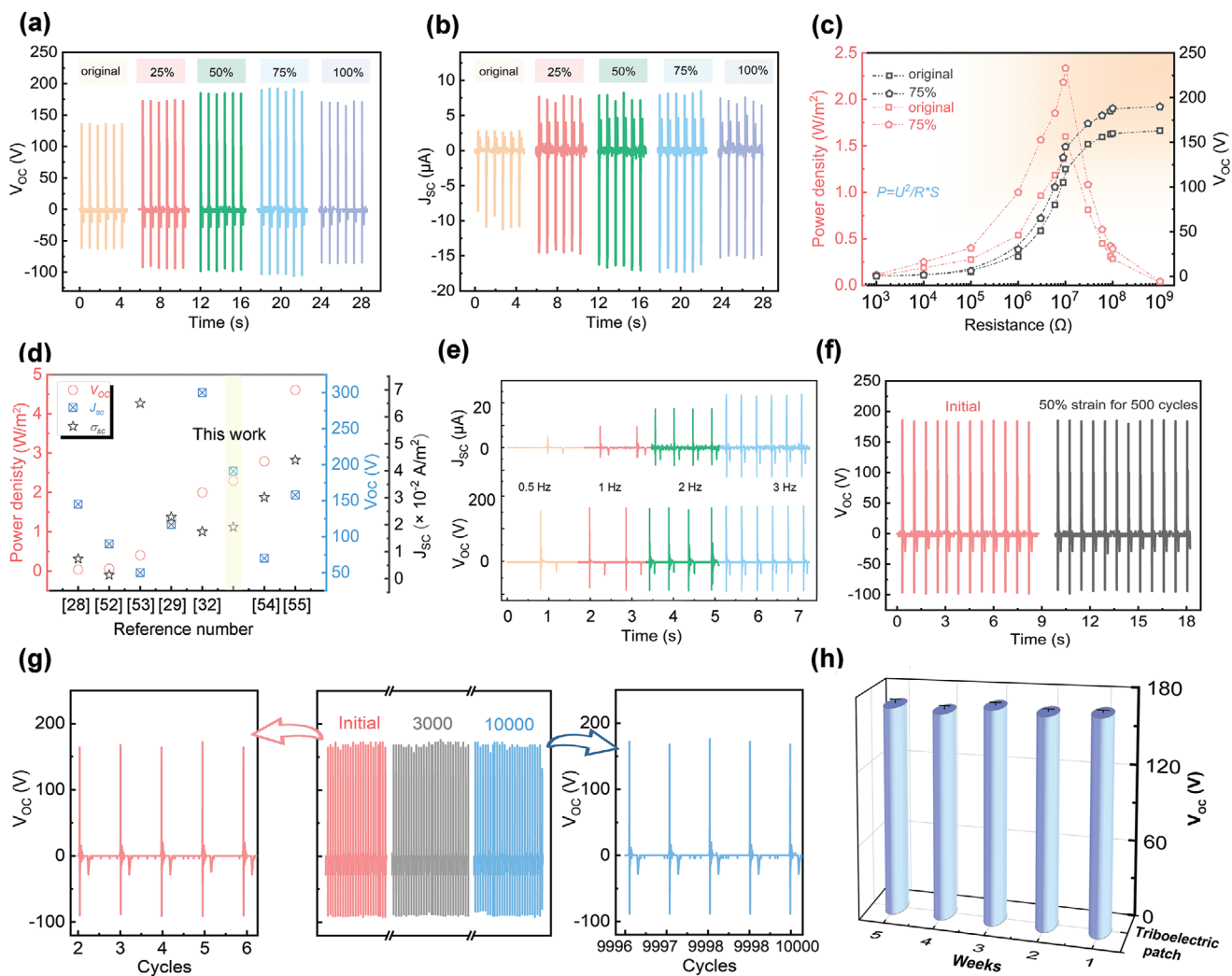


**Figure 5.** The electrical performance and durability of the polyionic triboelectric patch. The a)  $V_{OC}$  and  $J_{SC}$  b) outputs under different tensile strains. c) Dependence of the output voltage and instantaneous power density on load resistance. d) Comparison with recent important works on ionic conductor/electrolyte-based TENGs. e) The  $V_{OC}$  and  $J_{SC}$  output versus frequencies. f) The output voltage of the device at 50% strain for 500 cycles. Stability of output voltage under operations for g) 10 000 cycles and h) within 5 weeks.

the LED remains stable brightness (Figure S11 and Video S4, Supporting Information). The  $\sigma_{SC}$  output of devices presents the same trend as that of  $J_{SC}$  output (Figure S12, Supporting Information). The  $V_{OC}$ ,  $J_{SC}$ , and  $\sigma_{SC}$  of triboelectric patch versus PA content are intuitively displayed in Figure 4i. It is observed that the PA content of 1 mL is a critical point for the enhancement in electrical output and the device achieves the  $V_{OC}$  of 163 V,  $J_{SC}$  of 13.8  $\mu A$ , and  $\sigma_{SC}$  of 47 nC, which are 3.0 times, 4.9 times, and 4.3 times higher than that of the device with the only copper wire electrode, respectively. Considering both the electrical output and adhesion, the triboelectric patch with the PA content of 5 mL is used for the subsequent study.

#### 2.4. Electrical Output and Durability

Owing to the extensibility of triboelectric patch, the electrical performance at various tensile strain levels was evaluated in

Figure 5a,b and Figure S13 (Supporting Information). When the strain increases from 0% to 100%, the electrical outputs present an increase and then a slight decrease. The device generates the maximum output signals with the  $V_{OC}$  of 191 V and  $J_{SC}$  of 17.3  $\mu A$  at 75% tensile strain. This change is related to the coupling effect between tribolayer thickness and effective contact area. For one thing, due to Poisson's effect, the thickness of LTV tribolayer can be thinned under uniaxial strain (Figure S14, Supporting Information), resulting in a larger device capacitance.<sup>[22]</sup> For another, the frictional contact area can be enlarged with the increase of tensile strain under low tension state (<75%), which can exert a positive effect on the increase of electrical output of triboelectric patch. However, as the tensile strain further increases, the frictional contact area decreases, thus resulting in the degradation of electrical outputs (Note S1, Supporting Information).

Furthermore, the electrical performance of triboelectric patch strongly depends on external resistors. Figure 5c

investigated output voltage and power density under various load resistances. As the resistance increases from  $10^3$  to  $10^9 \Omega$ , the output voltage of devices also increases, which follows Ohm's law. And the power output is calculated by the equation of  $P = \frac{U^2}{RS}$ , where  $S$ ,  $R$ , and  $U$  are contact area, load resistance, and output voltage, respectively. The power density of device (75%) can be up to  $2.3 \text{ W m}^{-2}$  at the load resistance of  $10 \text{ M}\Omega$ , which is compared to or higher than reported ionic conductor/electrolyte-based TENGs (Figure 5d).<sup>[28,29,32,52–55]</sup> Furthermore, the electrical performance under various operating frequencies was examined in Figure 5e. The  $V_{OC}$  of the device shows a stable value, while the  $J_{SC}$  exhibits an upward tendency due to free electrons flowing for equilibrium in a shorter time.<sup>[56]</sup> Moreover, the triboelectric patch can collocate with daily-used fabrics to provide considerable electricity, as demonstrated in Figure S15 in the Supporting Information. When the patch rubs against nylon fabric, the maximum output voltage of triboelectric patch can be obtained. Note that the output amplitude depends on the electronegativity difference of tribopairs.

The output stability and robustness are key attributes of wearable electronics for long-term use. As shown in Figure 5f, after being stretched for 500 cycles at 50% strain, the triboelectric patch displays an output voltage similar to the initial value. And no degradation of electrical output even after dynamic folding and twisting for many times. (Figure S16, Supporting Information). The illustration shows photos of triboelectric patches in folded and twisted states. Moreover, the electrical output of device was examined under 10 000 times contact-separation movements or long-term exposure to atmospheric environment in Figure 5g,h. The corresponding outputs are nearly comparable to the initial value, without measurable fluctuation. These measurements indicate good output stability and durability of triboelectric patch, which can provide a guarantee in a real-world application.

## 2.5. Potential Applications

Owing to its electrical performance, adhesiveness, stretchability, and optical transparency, the triboelectric patch possesses promising applications in the wearable system. To explore the potential as a wearable power source, the charging behavior of triboelectric patches across commercial capacitors was investigated in Figure 6a and Figure S17 in the Supporting Information. Capacitors with lower capacitance show a faster charging rate for the same charging potential. Especially, the capacitor of  $1 \mu\text{F}$  can be charged to  $\approx 8 \text{ V}$  within only 1 min, demonstrating the rapid charging ability. Figure 6b records charging voltage-time curves of capacitors at different frequencies. The higher the operating frequency of triboelectric patch, the faster the charging speed. The charging speed for capacitor at 2.5 Hz is about seven times higher than that at 0.5 Hz. Moreover, the charging/discharging curve of a capacitor is given in Figure 6c. The charging voltage quickly reaches 2.6 V in 150 s, at which point a LED can be lit up successfully, which indicates the practical feasibility of using the triboelectric patch to power microelectronics. Considering its application in real wearability, the electricity production capacity of triboelectric patch under tailoring and dynamic stretching

conditions was checked. As shown in Figure 6d, when the patch is cut out with a square hole, the pentagonal LED logo can still be driven to full brightness by tapping the patch periodically. The demonstration shows that solid-state triboelectric patches can be customized according to the user's requirements, which is superior to other TENG devices containing liquid electrolyte or ionic liquid. Figure 6e and Video S5 (Supporting Information) present that the triboelectric patch can almost completely return to its initial state after being highly stretched and the LED logo can be still lit.

The triboelectric patch can be used not only as a wearable power source but also as a self-powered tactile sensor. As shown in Figure S18 (Supporting Information), the amplitude of electrical signal increases with the increase of touch pressure and the frequency of output is identical to the touch frequency of the index finger, exhibiting quick pressure response. A designed triboelectric patch array ( $1 \times 3$  units, noted as  $N_1$ ,  $N_2$ ,  $N_3$ ) can be autonomously attached to daily-used clothes, as shown in Figure 6f–i. When the index finger presses each unit in turn, corresponding touch signals are detected (Figure 6g,h) and meanwhile the fingertip pressure can be converted into electricity for lighting up corresponding LED array (Figure 6 f-ii–iv). In addition, a sensing bracelet was designed by sticking the triboelectric patch strip ( $180 \times 12 \text{ mm}^2$ ) to the inner circumferential surface of commercial bracelet. Note that it is not necessary to use adhesives such as tape. The sensing bracelet is capable of quickly responding to various mechanical stimuli in multiple directions. As shown in Figure 6i–i, as the number of pressed fingers changes to one, two, and three in sequence, the signal amplitude perceived by bracelet gradually enlarges (Video S6, Supporting Information). This is because the contact area under three fingers pressure is the largest, resulting in more tribocharges between human skin and the inner surface of bracelet. This sensing bracelet is further capable of monitoring the strength of clapping hand. As shown in Figure 6i–ii and Video S7 (Supporting Information), the amplitude of detected signal strongly depends on the clapping force, exhibiting an approximately linear relationship (Figure S19, Supporting Information). Moreover, the sensing bracelet presents electrical signals with different amplitudes and frequencies in response to repeated hand gripping, knocking, and shaking motions (Figure 6i–iii; Video S8, Supporting Information). By distinguishing these signals, the motion state of human hand can be roughly inferred. Additionally, the triboelectric patch is also used as a wearable input device or touchpad for user interface system. As shown in Figure 6j–i–iii, and Video S9 (Supporting Information), the triboelectric patch ( $3 \times 3 \text{ cm}^2$ ) attached to the arm could sense the touch pressure from index fingertip. And the acquired touch signal was then transmitted to the relay as a trigger signal. The driven control for terminal application, including daylight lamp, electric fan, and mobile phone powering, was thus realized successfully. The corresponding circuit diagram is described in Figure S20 (Supporting Information). Figure 6k records the corresponding trigger voltage of about 5 V. These demonstrations of sensing bracelet and soft touchpad imply that the triboelectric patch has a bright prospect in the field of self-powered sensing systems and human-machine interactions.

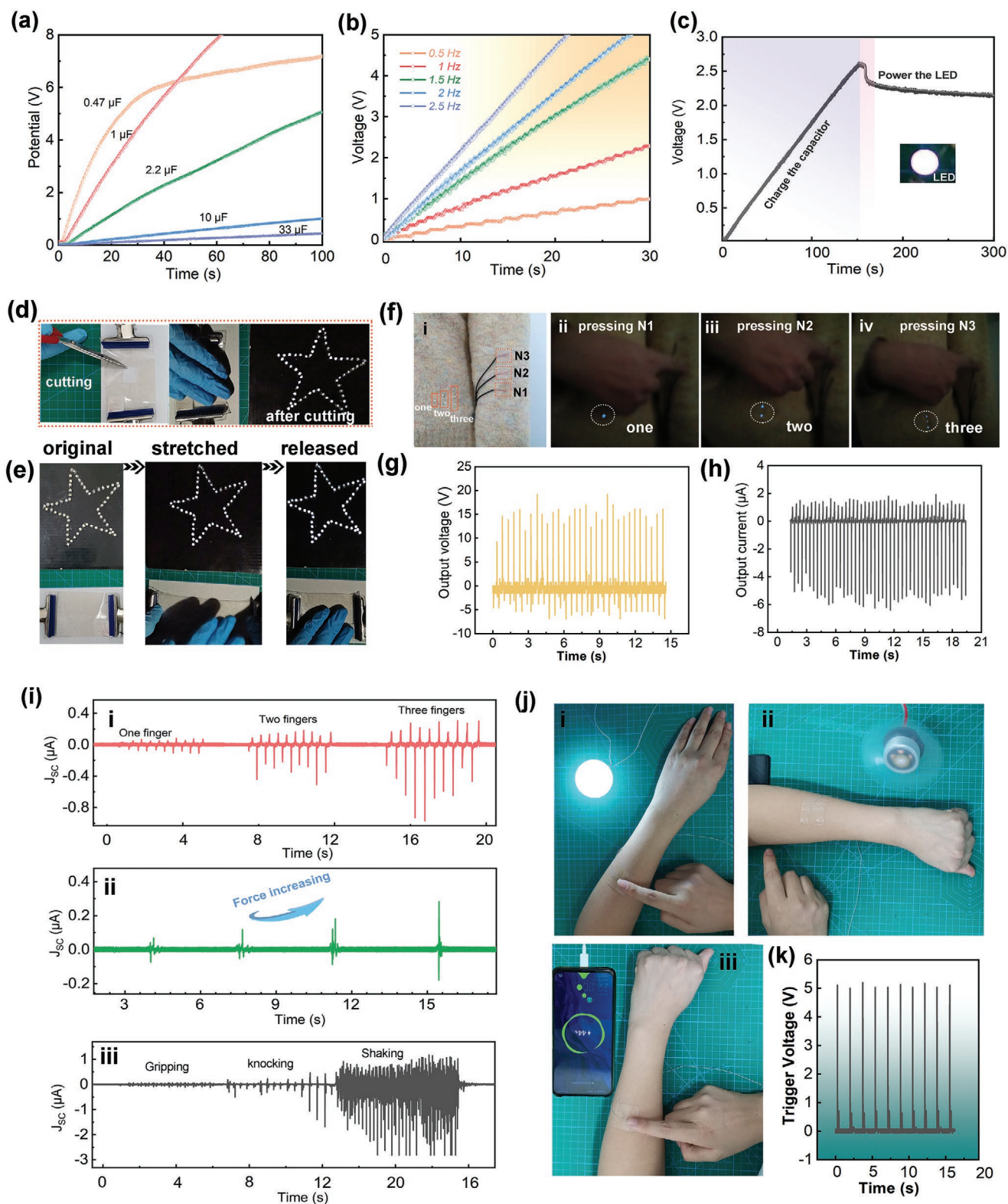


**Figure 6.** The potential application of solid-state triboelectric patch for wearable power source, motion monitoring, and user interface system. a) Charging curves of different capacitors. b) Charging behavior of device at different frequencies. c) Real-time charge–discharge curve. Photographs demonstrating that the device could drive LED arrays under d) dynamic tailoring or e) stretching conditions. f) The designed patch array attached to clothes was used to sense fingertip pressure and supply power for LEDs. Sensing g) voltage and h) current of patch unit under finger pressing. i) Perception of thrust area i-i), pressure intensity i-ii), and hand motion i-iii) by triboelectric patch-based sensing bracelet. j) Intelligently control for lamp j-i), fan j-ii), and mobile phone j-iii) by triboelectric patch as the touchpad. k) The trigger output from the touchpad.

### 3. Conclusion

In summary, an extensible, adhesive, and transparent triboelectric patch with PWP polyionic electrode was proposed using simple solution processing method. The patch exhibits an average transmittance of over 85% in the visible region, adhesive strength of 44.3 N m<sup>-1</sup> to silk fabric, and breaking elongation of 318%. The optimal device is achieved using the PWP composite with 5 mL PA content and thickness of 85 μm. And the patch working in the single-electrode mode can generate high output  $V_{OC}$  of 191 V and  $J_{SC}$  of 17.3 μA. This is the first time that robust solid-state TENG possesses these characteristics at the same time. The patch can be easily attached to various nonplanar substrates for further harvesting biomechanical energies, charging capacitors, driving electronics, and detecting physiological movements. Additionally, the triboelectric patch can be used as a soft touchpad to control electrical appliances including mobile phones, commercial lamps, electric fans. Importantly, the patch can retain good output stability and durability after repeated stretching/twisting/folding cycles or numerous contact-separation movements or tailoring conditions. Consequently, this solid-state and liquid-free triboelectric patch is expected to show great potential in E-skins, human-machine interactions, soft robots, optoelectronic devices, and other fields.

### 4. Experimental Section

**Fabrication of PWP Current Collector:** The 10 wt% PEO was prepared by dissolving PEO powder (average  $M_v = 100\,000$ , Sigma-Aldrich) into deionized (DI) water. Subsequently, the WPU solution (WPU-2601XP) was added and further stirred to obtain homogeneous blended solution. The mass ratio of PEO to WPU was fixed at 1:0.5. Afterward, taking different volumes (0.2, 0.4, 0.6, 0.8, 1.0, 3.0, 5.0 mL) of PA solution (>70% content) and diluting them to the fixed volume (5.0 mL) with DI water and adding these PA solutions into the above PEO/WPU mixture, separately. The PWP composites were prepared by blade-coating the PEO/WPU/PA solution into a preprepared groove model and then performing heat treatment at 55 °C for precurving.

**Assembling of the Triboelectric Patch:** The triboelectric patch was fabricated using the dry transfer technique. First, LTV silicon rubber mixture consisting of base agent and curing agent at a weight ratio of 1:1 was cast on the surface of pre-dried PWP composite and then cured in an oven at 50 °C. The PWP composite was naturally transferred onto the surface of LTV tribolayer when the tribolayer was detached from the pre-prepared groove model. Finally, copper wire was placed under the PWP layer for subsequent electrical connection.

**Materials Characterization:** The microscopic architecture and cross-sectional morphology were characterized by field-emission scanning electron microscope (FE-SEM, Hitachi SU8010). The optical transmittance was investigated using a UV-vis near-infrared spectrophotometer. The surface chemical structure was characterized using attenuated total reflectance Fourier transform infrared spectroscopy (ATR-FTIR). The X-ray diffraction pattern was performed on an X-ray diffraction spectroscopy by using Cu K $\alpha$  radiation ( $\lambda = 1.5406$  Å). Contact Angle Analyzer (OCA15EC, German) was used to measure water contact angle.

**Adhesive Strength Characterization:** The adhesion strength of triboelectric patch was measured via 90° delamination test at 20 °C and 65% relative humidity. Cotton, silk, flax, nylon fabric, paper, rubber, and PTFE plastic were used as typical testing substrates. These substrates were fixed on the testing machine. Strip samples adhered onto the substrates were delaminated perpendicularly to the substrate

at a constant peeling speed of 5 mm min<sup>-1</sup>. The adhesive strength was determined by dividing the average stable load by the width of the triboelectric patch. Three samples were tested for each group.

**Mechanical and Electrical Performance Measurement:** All samples were cut into rectangular for mechanical tensile testing on a multifunctional tensile machine. The cyclic loading-unloading tensile test was conducted to evaluate the elasticity of the triboelectric patch. The impedance spectroscopy was recorded by an electrochemical workstation. Ionic conductivity of PWP composite was calculated according to the formula of  $\sigma = \frac{d}{A \times R_b}$ , where  $d$  is the thickness of samples,  $A$  is the area of samples, and the  $R_b$  is the bulk resistance from the Nyquist plots of impedance spectrum. The output voltage, current, and charge were measured using digital oscilloscope and programmable electrometer. All human subjects gave written and informed consent before participation in the experiments.

### Supporting Information

Supporting Information is available from the Wiley Online Library or from the author.

### Acknowledgements

This work was financially supported by the Fundamental Research Funds for the Central Universities and Graduate Student Innovation Fund of Donghua University [Grant number BCZD2021001 and CUSF-DH-D-2020007]. Z.B. would also like to acknowledge the fellowship from the China Scholarship Council (CSC) under the Grant CSC No. 202006630049.

### Conflict of Interest

The authors declare no conflict of interest.

### Data Availability Statement

Research data are not shared.

### Keywords

adhesiveness, polyionic composites, power sources, tactile sensors, triboelectric nanogenerators

Received: May 8, 2021

Revised: June 17, 2021

Published online:

- [1] J. Sun, X. Pu, M. Liu, A. Yu, C. Du, J. Zhai, W. Hu, Z. L. Wang, *ACS Nano* **2018**, *12*, 6147.
- [2] Z. Bai, Z. Zhang, J. Li, J. Guo, *Nano Energy* **2019**, *65*, 104012.
- [3] A. Petritz, E. Karner-Petritz, T. Uemura, P. Schaffner, T. Araki, B. Stadlober, T. Sekitani, *Nat. Commun.* **2021**, *12*, 2399.
- [4] I. Kim, H. Roh, J. Yu, N. Jayababu, D. Kim, *ACS Energy Lett.* **2020**, *5*, 1577.
- [5] L. F. F. G. Massimo Mariello, *Adv. Funct. Mater.* **2021**, 2101047.
- [6] B. Dong, Q. Shi, Y. Yang, F. Wen, Z. Zhang, C. Lee, *Nano Energy* **2021**, *79*, 105414.

- [7] J. Yun, N. Jayababu, D. Kim, *Nano Energy* **2020**, *78*, 105325.
- [8] B. Lee, J. Y. Oh, H. Cho, C. W. Joo, H. Yoon, S. Jeong, E. Oh, J. Byun, H. Kim, S. Lee, J. Seo, C. W. Park, S. Choi, N. M. Park, S. Y. Kang, C. S. Hwang, S. D. Ahn, J. I. Lee, Y. Hong, *Nat. Commun.* **2020**, *11*, 663.
- [9] J. Wen, J. Tang, H. Ning, N. Hu, Y. Zhu, Y. Gong, C. Xu, Q. Zhao, X. Jiang, X. Hu, L. Lei, D. Wu, T. Huang, *Adv. Funct. Mater.* **2021**, *31*, 2011176.
- [10] J. Tao, S. Zhongda, L. Long, Z. Quan, Z. Minglu, Z. Zixuan, Y. Guangjie, C. Tao, T. Yingzhong, H. Xuyan, L. Chengkuo, *Nat. Commun.* **2020**, *11*, 5381.
- [11] H. Jinno, T. Yokota, M. Koizumi, W. Yukita, M. Saito, I. Osaka, K. Fukuda, T. Someya, *Nat. Commun.* **2021**, *12*, 2234.
- [12] X. Shi, Y. Zuo, P. Zhai, J. Shen, Y. Yang, Z. Gao, M. Liao, J. Wu, J. Wang, X. Xu, Q. Tong, B. Zhang, B. Wang, X. Sun, L. Zhang, Q. Pei, D. Jin, P. Chen, H. Peng, *Nature* **2021**, 591, 240.
- [13] Q. Li, A. Zanelli, *Renewable Sustainable Energy Rev.* **2021**, *139*, 110678.
- [14] J.-Y. Sun, C. Keplinger, G. M. Whitesides, Z. Suo, *Adv. Mater.* **2014**, *26*, 7608.
- [15] L. A. Wehner, N. Mittal, T. Liu, M. Niederberger, *ACS Cent. Sci.* **2021**, *7*, 231.
- [16] Z. L. Wang, *Mater. Today* **2017**, *20*, 74.
- [17] H. Wang, M. Han, Y. Song, H. Zhang, *Nano Energy* **2021**, *81*, 105627.
- [18] S. Adonijah Graham, B. Dudem, H. Patnam, A. R. Mule, J. S. Yu, *ACS Energy Lett.* **2020**, *5*, 2140.
- [19] S. Maiti, S. K. Karan, J. K. Kim, B. B. Khatua, *Adv. Energy Mater.* **2019**, *9*, 1803027.
- [20] M. Wu, Z. Gao, K. Yao, S. Hou, Y. Liu, D. Li, J. He, X. Huang, E. Song, J. Yu, X. Yu, *Mater. Today Energy* **2021**, *20*, 100657.
- [21] Z. Bai, Y. Xu, J. Li, J. Zhu, C. Gao, Y. Zhang, J. Wang, J. Guo, *ACS Appl. Mater. Interfaces* **2020**, *12*, 42880.
- [22] Y.-C. Lai, J. Deng, S. Niu, W. Peng, C. Wu, R. Liu, Z. Wen, Z. L. Wang, *Adv. Mater.* **2016**, *28*, 10024.
- [23] B. S. Kim, H. Kwon, H. J. Kwon, J. B. Pyo, J. Oh, S. Y. Hong, J. H. Park, K. Char, J. S. Ha, J. G. Son, S. S. Lee, *Adv. Funct. Mater.* **2020**, *30*, 1910214.
- [24] Y. Chen, X. Pu, M. Liu, S. Kuang, P. Zhang, Q. Hua, Z. Cong, W. Guo, W. Hu, Z. L. Wang, *ACS Nano* **2019**, *13*, 8936.
- [25] S. Chen, T. Huang, H. Zuo, S. Qian, Y. Guo, L. Sun, D. Lei, Q. Wu, B. Zhu, C. He, X. Mo, E. Jeffries, H. Yu, Z. You, *Adv. Funct. Mater.* **2018**, *28*, 1805108.
- [26] X. Jing, H. Li, H.-Y. Mi, P.-Y. Feng, X. Tao, Y. Liu, C. Liu, C. Shen, *ACS Appl. Mater. Interfaces* **2020**, *12*, 23474.
- [27] Y. C. Lai, H. M. Wu, H. C. Lin, C. L. Chang, H. H. Chou, Y. C. Hsiao, Y. C. Wu, *Adv. Funct. Mater.* **2019**, *29*, 1904626.
- [28] J. Wang, J. Shi, X. Deng, L. Xie, J. Jiang, J. Tang, J. Liu, Z. Wen, X. Sun, K. Liu, Y. Fang, *Nano Energy* **2020**, *78*, 105348.
- [29] L. Sun, S. Chen, Y. Guo, J. Song, L. Zhang, L. Xiao, Q. Guan, Z. You, *Nano Energy* **2019**, *63*, 103847.
- [30] Y. Yang, J. Han, J. Huang, J. Sun, Z. L. Wang, S. Seo, Q. Sun, *Adv. Funct. Mater.* **2020**, *30*, 1909652.
- [31] C. Dong, A. Leber, G. T. Das, R. Chandran, M. Volpi, Y. Qu, T. Nguyen-Dang, N. Bartolomei, W. Yan, F. Sorin, *Nat. Commun.* **2020**, *11*, 3537.
- [32] L. Wang, W. Liu, Z. Yan, F. Wang, X. Wang, *Adv. Funct. Mater.* **2021**, *31*, 2007221.
- [33] J.-N. Kim, J. Lee, H. Lee, I.-K. Oh, *Nano Energy* **2021**, *82*, 105705.
- [34] L. Wang, W. A. Daoud, *Nano Energy* **2019**, *66*, 104080.
- [35] S. C. B. Mannsfeld, B. C.-K. Tee, R. M. Stoltenberg, C. V. H.-H. Chen, S. Barman, B. V. O. Muir, A. N. Sokolov, C. Reese, Z. Bao, *Nat. Mater.* **2010**, *9*, 859.
- [36] C. Larson, B. Peele, S. Li, S. Robinson, M. Totaro, L. Beccai, B. Mazzolai, R. Shepherd, *Science* **2016**, *351*, 1071.
- [37] Z. Tashi, M. Zare, N. Parvin, *Mater. Lett.* **2020**, *264*, 127275.
- [38] J. Zhang, W. Tu, Z. Dai, *Prog. Org. Coat.* **2012**, *75*, 579.
- [39] K. Y. Lee, J. Chun, J.-H. Lee, K. N. Kim, N.-R. Kang, J.-Y. Kim, M. H. Kim, K.-S. Shin, M. K. Gupta, J. M. Baik, S.-W. Kim, *Adv. Mater.* **2014**, *26*, 5037.
- [40] H. L. Wang, Z. H. Guo, G. Zhu, X. Pu, Z. L. Wang, *ACS Nano* **2021**, *15*, 7513.
- [41] N. An, X. Wang, Y. Li, L. Zhang, Z. Lu, J. Sun, *Adv. Mater.* **2019**, *31*, 1904882.
- [42] J. Mattia, P. Painter, *Macromolecules* **2007**, *40*, 1546.
- [43] F.-K. Shi, X.-P. Wang, R.-H. Guo, M. Zhong, X.-M. Xie, *J. Mater. Chem. B* **2015**, *3*, 1187.
- [44] Y. Yang, Z. Ye, X. Liu, J. Su, *J. Mater. Chem. C* **2020**, *8*, 5280.
- [45] B. T. Michal, E. J. Spencer, S. J. Rowan, *ACS Appl. Mater. Interfaces* **2016**, *8*, 11041.
- [46] L. Zhang, K. S. Kumar, H. He, C. J. Cai, X. He, H. Gao, S. Yue, C. Li, R. C.-S. Seet, H. Ren, J. Ouyang, *Nat. Commun.* **2020**, *11*, 1.
- [47] C. Yang, W. Lin, Z. Li, R. Zhang, H. Wen, B. Gao, G. Chen, P. Gao, M. M. F. Yuen, C. P. Wong, *Adv. Funct. Mater.* **2011**, *21*, 4582.
- [48] S. Yang, Y. Zhang, G. Yuan, X. Zhang, J. Xu, *Macromolecules* **2004**, *37*, 10059.
- [49] Q. Zhang, X. Liu, L. Duan, G. Gao, *J. Mater. Chem. A* **2020**, *8*, 4515.
- [50] Z. Lei, P. Wu, *Mater. Horiz.* **2019**, *6*, 538.
- [51] T. Jing, B. Xu, Y. Yang, M. Li, Y. Gao, *Nano Energy* **2020**, *78*, 105373.
- [52] P. Zhang, Y. Chen, Z. H. Guo, W. Guo, X. Pu, Z. L. Wang, *Adv. Funct. Mater.* **2020**, *30*, 1909252.
- [53] K. Parida, V. Kumar, W. Jjiangxin, V. Bhavanasi, R. Bendi, P. S. Lee, *Adv. Mater.* **2017**, *29*, 1702181.
- [54] L. Wang, W. A. Daoud, *Adv. Energy Mater.* **2018**, *9*, 1803183.
- [55] Y. Wu, Y. Luo, J. Qu, W. A. Daoud, T. Qi, *Nano Energy* **2020**, *75*, 105027.
- [56] X.-S. Zhang, M.-D. Han, R.-X. Wang, F.-Y. Zhu, Z.-H. Li, W. Wang, H.-X. Zhang, *Nano Lett.* **2013**, *13*, 1168.